Operando Spectroscopic Analysis of Axial Oxygen-Coordinated Single-Sn-Atom Sites for Electrochemical CO2 Reduction

Yachen Deng, Jian Zhao, Shifu Wang, Ruru Chen, Jie Ding, Hsin-Jung Tsai, Wen-Jing Zeng, Sung-Fu Hung, Wei Xu, Junhu Wang, et al.

Operando Spectroscopic Analysis of Single-Sn-Atom Material for Electrochemical CO_2 Reduction

Yachen Deng[a,b,1], Jian Zhao[a,1], Shifu Wang[a,c,1], Ruru Chen [a,c], Hsin-Jung Tsai[d], Wen-Jing Zeng[d], Sung-Fu Hung[d], Wei Xu[e,f], Junhu Wang[g], Frédéric Jaouen[h], Xuning Li[a,b,*], Yanqiang Huang[a,b,*] and Bin Liu[i,*]

[a]*State Key Laboratory of Catalysis, Dalian Institute of Chemical Physics, Chinese Academy of Sciences, Dalian 116023, P.R. China.*

[b]*University of Chinese Academy of Sciences, Beijing 100049, P.R. China.*

[c]*Department of Chemical Physics, University of Science and Technology of China, Hefei 230026, P.R. China.*

[d]*Department of Applied Chemistry, National Yang Ming Chiao Tung University, Hsinchu 300, Taiwan.*

[e]*Beijing Synchrotron Radiation Facility, Institute of High Energy Physics, Beijing 100049, P.R. China.*

[f]*RICMASS, Rome International Center for Materials Science Superstripes, Rome 00185, Italy.*

[g]*Center for Advanced Mössbauer Spectroscopy, Mössbauer Effect Data Center, Dalian Institute of Chemical Physics, Chinese Academy of Sciences, Dalian 116023, P.R. China.*

[h]*Institut Charles Gerhardt Montpellier, University of Montpellier, CNRS, ENSCM, Montpellier 34095, France.*

[i]*School of Chemical and Biomedical Engineering, Nanyang Technological University, 62 Nanyang Drive, Singapore 637459, Singapore.*

*Corresponding Authors:

lixn@dicp.ac.cn (X.L)

yqhuang@dicp.ac.cn (Y.H)

liubin@ntu.edu.sg (B.L)

Abstract

Sn-based materials have been demonstrated as promising catalysts for selective electrochemical CO_2 reduction reaction (CO_2RR). However, the detailed structures of catalytic intermediates and the key surface species remain to be identified. In this work, a series of single-Sn-atom catalysts with well-defined structures are developed as model systems to explore their electrochemical reactivity towards CO_2RR . The selectivity and activity of CO_2 reduction to formic acid on Sn single-atom sites are shown to be correlated with Sn(IV)-N_4 moieties axially coordinated with oxygen (O-Sn-N_4). Employing a combination of *operando* X-ray absorption spectroscopy, attenuated total reflectance surface enhanced infrared absorption spectroscopy, Raman spectroscopy and ^{119}Sn Mössbauer spectroscopy, surface-bound bidentate tin carbonate species are precisely captured during CO_2RR. Moreover, the electronic and coordination structure of the single-Sn-atom species under reaction conditions are accurately determined. Density functional theory (DFT) calculations further supports the preferred formation of Sn-O-CO_2 species over the O-Sn-N_4 sites, which effectively modulates the adsorption configuration of the reactive intermediates and lowers the energy barrier for the hydrogenation of *OCHO species, as compared to the preferred formation of *COOH species over the Sn-N_4 sites, thereby greatly facilitating CO_2-to-HCOOH conversion.

Introduction

The overdependence on fossil fuels leads to an excessive accumulation of greenhouse gas in the atmosphere. It is urgent to develop highly efficient and environmentally friendly technologies to mitigate the depletion of fossil resources, abate carbon emission and to switch to renewable resources.[1-5] Electrocatalytic carbon dioxide reduction reactions (CO_2RRs) offer sustainable opportunities to transform CO_2 into value-added chemicals and carbon-based fuels.[6-8] While various products can be produced from CO_2RR, some of the C1 products (i.e. formic acid and CO) can be obtained with high selectivity and high energy efficiency, and are of great interest to the chemical industry.[9-12] Formic acid (HCOOH) is widely explored as a hydrogen storage material and chemical fuel for fuel cells.[13-15] Until now, electrocatalysts developed for reducing CO_2 to HCOOH have included noble metals (e.g., Pd) and transitional-metal-based materials (e.g., Cu, Bi, Pb, In, Sn etc).[16-22]

Owing to their unique electronic structure, Sn-based materials have been identified as attractive catalysts for electrochemical CO_2 reduction to HCOOH and/or CO,[23] but suffer from insufficient selectivity and activity, especially at large cathodic current densities.[24] To this end, past researches focused on doping Sn crystalline phases with other metal or nonmetal elements to tune the electron density at the Sn active sites and their neighboring dopants to selectively stabilize the reaction intermediates and improve the activity and selectivity of CO_2RR.[19, 25-29] However, the complex structure model and the complicated coordination environment of metal sites make it difficult to capture the intermediate species and determine the true active sites during the reaction process.

Single-atom catalysts (SACs) with well-defined and atomically-dispersed metal sites, tunable coordination environment and high utilization efficiency, have shown promising CO_2RR activity and selectivity towards CO, especially Fe-N-C and Ni-N-C materials.[30 31] This class of materials provides an ideal platform for exploring the structure of active sites and understanding structure-activity relationships.[32-37] Beyond 3d transition metal SACs, early studies reported that single-Sn-atom sites in

Sn-SACs could selectively reduce CO_2 either to HCOOH or CO.[2, 10 38] To reveal the intrinsic origin for the different CO_2RR selectivity of Sn-single-atom sites, it is necessary to pinpoint the exact electronic and coordination structure of the catalytic species under CO_2RR conditions. This in turn requires the rational design of single-Sn-atom materials with well-defined sites and the development of advanced *operando* characterization tools with atomic resolution.

In this work, a series of Sn-N-C catalysts featuring single-Sn-atoms with tunable and well-defined coordination environments were developed. The average Sn(IV)/Sn(II) ratio could be modulated via the functionalization of carbon nanotubes, modifying the adsorption energy of Sn phthalocyanine (SnPc) molecules. In particular, a model single-Sn-atom catalyst with ~100% axially oxygen coordinated Sn(IV) species (O-Sn-N_4) was obtained using OH-functionalized carbon nanotubes, showing the optimal catalytic activity and selectivity towards HCOOH. Taking advantages of *operando* attenuated total reflectance surface enhanced infrared absorption spectroscopy (ATR-SEIRAS) and Raman spectroscopy, a surface-bound bidentate tin carbonate species was revealed as a key reaction intermediate during CO_2RR. *Operando* ^{119}Sn Mössbauer spectroscopy was applied for the first time to follow changes in the electronic and coordination structure of single-Sn-atom species under CO_2RR. In combination with *operando* X-ray absorption spectroscopy (XAS), the *in situ* generation of the Sn-O-CO_2 catalytic intermediate during CO_2RR was clearly identified. Density functional theory (DFT) calculations further evidenced the dynamic evolution of the electronic structure of O-Sn-N_4 site for CO_2RR and the catalytic mechanism over single-Sn-atom species was unveiled at atomic scale.

Results and discussion

Characterization of the single–Sn-atom catalysts

A series of single-Sn-atom catalysts were prepared by immobilizing SnPc molecules on CNTs subjected to different functionalization treatments (CNT, CNT-OH and CNT-NH_2) via π-π

interaction.[39] The respective electrocatalysts are labelled SnPc/CNT, SnPc/CNT-OH and SnPc/CNT-NH_2. The synthesis of SnPc/CNT-OH is schemed in **Fig. 1a**, and fully detailed in **Methods** and **Supplementary Fig. 1**. The X-ray diffraction (XRD) patterns of this series of materials show only one diffraction peak assignable to the diffraction line of carbon nanotubes, suggesting that the SnPc molecules are well-dispersed and therefore cannot contribute to the diffraction patterns (**Supplementary Fig. 2)**. In contrast, Raman spectra display signals from both molecular SnPc and CNTs for all materials (**Supplementary Fig. 3**), indicating that SnPc was successfully loaded onto the CNTs. The Sn contents were in the range of 0.37-0.66 wt. % (**Supplementary Table 1)**. **Figure 1b** and **Supplementary Fig. 4** show representative scanning electron microscope (SEM) and transmission electron microscope (TEM) images of the catalysts, on which no aggregation of metal species could be observed. The surface morphology of SnPc/CNT-OH is similar to that of CNT-OH, indicating uniform dispersion of SnPc on CNT-OH, which is also confirmed by energy-dispersive X-ray spectroscopy (EDX) mapping analysis (**Supplementary Fig. 5**). Furthermore, high-angle annular dark-field scanning transmission electron microscopy (HAADF-STEM) image of SnPc/CNT-OH in **Fig. 1c** clearly shows Sn atoms dispersed on CNT and the absence of Sn clusters or nanoparticles, further suggesting the successful formation of single-Sn-atom catalysts.

X-ray photoelectron spectroscopy (XPS) was performed to examine the elemental compositions and Sn valence states of the single-Sn-atom catalysts. The Sn 3d XPS spectrum of the commercial SnPc can be deconvoluted into two peak groups assigned to Sn(II) (486.6 eV, 495 eV) and Sn(IV) (488.5 eV, 496.4 eV) (**Fig. 1d** and **Supplementary Fig. 6**).[40] For the series of catalysts, the Sn(IV)/Sn(II) ratio increases strongly in the order SnPc < SnPc/CNT-NH_2 < SnPc/CNT < SnPc/CNT-OH (**Supplementary Table 2** and **Supplementary Fig. 6**), with relative Sn(IV) amounts increasing from 18.1 % to 100 %. In particular, only Sn(IV) is observed for SnPc/CNT-OH (**Fig. 1e**), indicating that OH^- functional groups on CNT selectively lead to Sn(IV) possibly due to the strength of electrostatic interactions, which is supported by DFT calculations. As compared in **Supplementary**

Fig. 7, CNT-OH exhibits an adsorption energy for Sn(IV) species of -2.379 eV, more negative than those of CNT-NH_2 and CNT (-1.946 and -2.229 eV, respectively), suggesting that the CNT-OH surface more likely adsorbs Sn(IV) species than the other two types of carbon nanotubes.

To further determine the coordination environment and the electronic structure of the single-Sn-atom species, we conducted room temperature ^{119}Sn Mössbauer spectroscopy measurements. As shown in **Fig. 1f**, the commercial SnPc shows two quadrupole doublets with distinct values of isomer shift (IS) (0.03 and 2.72 mm s^{-1}) and quadrupole splitting (QS) (0.70 and 1.39 mm s^{-1}) (**Supplementary Table 3**). The doublets with low and high IS can unambiguously be assigned to Sn(IV) and Sn(II), respectively.[41] Moreover, the IS and QS values for the main high-IS doublet of the SnPc commercial product match well with those reported for Sn(II)Pc.[42] Interestingly, only one doublet with an IS value of 0.04 mm s^{-1} and a QS value of 0.50 mm s^{-1} was observed for SnPc/CNT-OH (**Fig. 1g**), which can be unambiguously assigned to Sn(IV) species. Based on IS and QS values calculated for a set of hypothetical site structures, the fitted parameters of this doublet match well with those calculated by DFT for the axially oxygen coordinated Sn(IV) species (O-Sn-N_4) structure (**Supplementary Fig. 8**).

As displayed in **Fig. 1h**, the absorption edge of Sn *K*-edge X-ray absorption near edge structure (XANES) spectrum of SnPc/CNT-OH shifts towards higher energies compared to that of SnPc, suggesting a higher average Sn valence state in the SnPc/CNT-OH catalyst,[26] in line with XPS analysis. The Fourier transforms of the extended X-ray absorption fine structure (EXAFS) spectra of both SnPc and SnPc/CNT-OH exhibit the dominant Sn-N coordination at 1.5-1.7 Å, distance not corrected for phase shift (**Supplementary Fig. 9**). No obvious peaks related to Sn-Sn coordination could be observed, confirming the atomic dispersion of all or most of the Sn atoms. In addition, the EXAFS spectra for SnPc and SnPc/CNT-OH could be well fitted with the structural models of Sn-N_4 and O-Sn-N_4 (as optimized from DFT), respectively (**Supplementary Fig. 10**). The fitted parameters are summarized in **Supplementary Table 4**. As depicted in **Fig. 1i** and **Supplementary Fig. 10**, the Sn atom in SnPc is coordinated, on average, with four adjacent N atoms (Sn-N_4), whereas the Sn atom in

SnPc/CNT-OH, on average, has four neighbouring N atoms and one axially coordinated O atom (O-Sn-N_4). All these results clearly show the successful development of a model single-Sn-atom catalyst with 100% axially oxygen coordinated Sn(IV) species anchored on OH-functionalized carbon nanotubes.

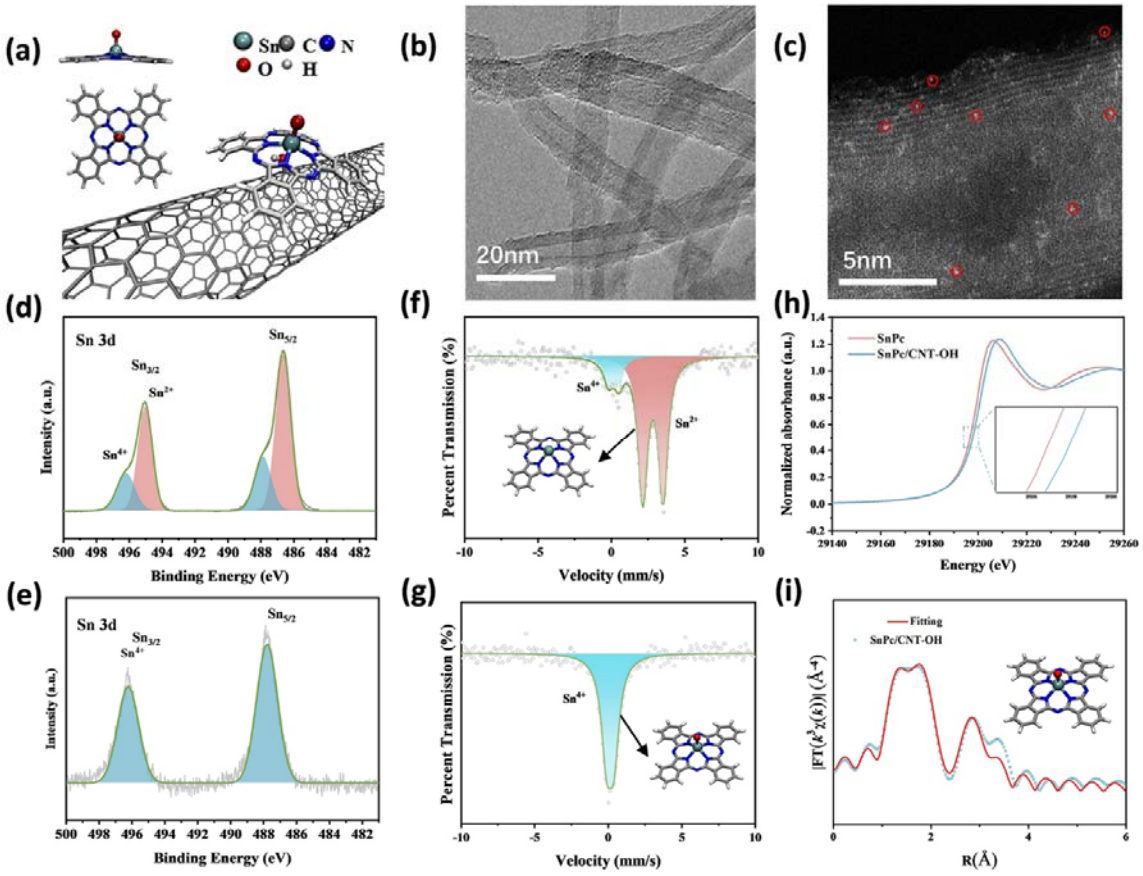

Fig. 1 | Structural characterization of the single-Sn-atom catalysts. a, Schematic illustration for the preparation of SnPc/CNT-OH. **b**, TEM and **c**, HAADF-STEM image of SnPc/CNT-OH. **d-e**, High-resolution Sn 3d XPS spectrum for SnPc and SnPc/CNT-OH, respectively. **f-g**, Room-temperature ^{119}Sn Mössbauer spectra for SnPc and SnPc/CNT-OH, respectively. **h**, Normalized Sn K-edge XANES spectra for SnPc and SnPc/CNT-OH (inset shows the Sn K-edge XANES spectra in a narrow region sensitive to the Sn oxidation state). **i**, Experimental and fitted EXAFS spectrum of SnPc/CNT-OH in *R* space.

Electrochemical CO_2RR performance

The electrochemical CO_2RR performance of SnPc/CNT, SnPc/CNT-OH and SnPc/CNT-NH_2 were examined in an H-type cell filled with CO_2-saturated 0.5 M $KHCO_3$ (pH = 7.3) electrolyte, and the CO_2RR catalyst loading was fixed at 1 mg·cm^{-2}.[43] The CO_2 reduction activity of the single-Sn-atom catalysts was first investigated by linear scan voltammetry (LSV) measurements. As shown in **Fig. 2a**, the current density for CO_2 reduction over SnPc/CNT-OH is the highest among this series of catalysts. **Fig. 2b** summarizes the potential-dependent CO_2RR Faradaic efficiency for SnPc/CNT, SnPc/CNT-OH and SnPc/CNT-NH_2. The main CO_2RR product is HCOOH, along with a small amount of CO, while H_2 is produced in significant quantities on all three catalysts. The HCOOH Faradaic efficiency over SnPc/CNT-OH can reach 75.4% at -1.13 V vs. RHE, which is higher than that over SnPc/CNT (48%) and SnPc/CNT-NH_2 (18%). The same trend is observed at other potentials, SnPc/CNT-OH systematically leading to higher FE towards HCOOH than the other two catalysts. As displayed in **Supplementary Fig. 11**, the SnPc/CNT-OH exhibits an optimal HCOOH partial current density (j_{HCOOH}) of -14.3 mA·cm^{-2} at -1.13 V vs. RHE, higher than that over SnPc/CNT (-5.2 mA·cm^{-2}) and SnPc/CNT-NH_2 (-2.4 mA·cm^{-2}). Besides excellent activity and selectivity, both the FE towards HCOOH and the current density remained nearly constant over SnPc/CNT-OH during 10 h at -1.13 V vs. RHE, indicating promising stability (**Fig. 2c**). The correlation of Faradaic efficiency, partial current density, and relative contents of Sn(II), Sn(IV) and nitrogen species are shown in **Fig. 2d** and **Supplementary Fig. 12**. The data reveals that the catalytic performance towards formic acid formation is positively correlated with the relative content of Sn(IV) (**Supplementary Fig. 12d**). This suggests that the Sn(IV) single atom species is the dominant catalytic site for electrochemical CO_2 reduction to formic acid, in line with recent reports.[44]

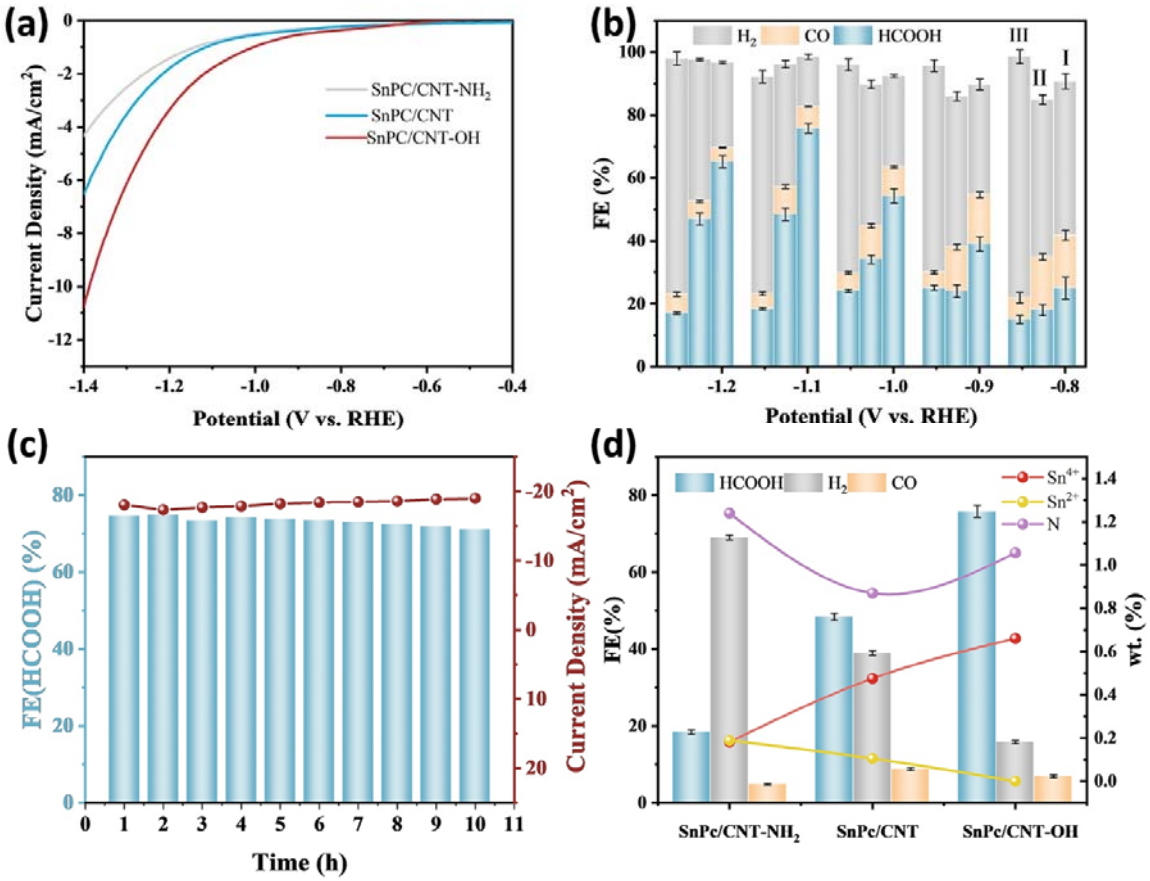

Fig. 2 | Electrochemical CO_2 reduction. a, LSV curves acquired on a rotating disc electrode in CO_2-saturated 0.5 M $KHCO_3$ solution. **b**, Faradaic efficiency of I: SnPc/CNT-OH, II: SnPc/CNT and III: SnPc/CNT-NH_2 at different applied cathodic potentials. **c**, Stability of SnPc/CNT-OH for CO_2RR at -1.13 V vs. RHE. **d**, Correlation diagram of the CO_2RR Faradaic efficiency and the relative contents of Sn(II), Sn(IV) and nitrogen species of SnPc/CNT, SnPc/CNT-OH and SnPc/CNT-NH_2: FE is indicated as columns (left-hand side y axis), while Sn(II), Sn(IV) and N content are indicated as curves (right-hand side y axis).

Identification of the catalytic intermediates and the surface reaction species

XRD, TEM and XPS characterizations of the SnPc/CNT-OH catalyst were performed and compared before and after CO_2RR, to investigate if an irreversible structural evolution occurred (**Supplementary Fig. 13-15**). Interestingly, no obvious morphology and valence state changes were

observed, further confirming the high stability of the SnPc/CNT-OH catalyst during the CO_2RR process.

To gain insights into the surface reaction intermediates over the single-Sn-atom catalyst during electrochemical CO_2 reduction to HCOOH, *operando* ATR-SEIRAS was carried out.[45] Control experiments were firstly conducted in Ar-saturated 0.1 M K_2SO_4 solution (**Supplementary Fig. 16**); only one peak centered at 1238 cm^{-1} was observed, which can be assigned to SO_4^{2-} in the electrolyte. During the potential stepping from 0 to -1.5 V vs. RHE and from -1.5 V vs. RHE to 0 in CO_2-saturated 0.1 M K_2SO_4 solution (pH = 4.5), the intensity of the absorption peak at 1650 cm^{-1} originating from water vibration was observed to slightly increase when stepping the potential from 0 to -1.5 V vs. RHE, and to decrease for the same potential step but in the opposite direction (**Fig. 3a and b*)***. The weak bands at 1950 and 2000 cm^{-1} are related to the linearly bonded CO (CO_L) because of the CO_2 to CO reaction pathway on CNT-OH (**Supplementary Fig. 17**). Additional absorption peaks at 1285 and 1115 cm^{-1} appeared at -0.8 V vs. RHE and their intensities increased when further decreasing the potential from -0.8 V to -1.5 V vs. RHE. These peaks can be ascribed to the C-O bond vibration in the bidentate tin carbonate.[46] The intensity of the tin carbonate peaks slowly decreased and finally disappeared when reverting the potential scan from -1.5 to 0 V vs. RHE. All these results clearly evidence the involvement of bidentate tin carbonate intermediates during the CO_2RR over SnPc/CNT-OH.

Operando Raman spectra recorded at varying potentials in CO_2- or Ar-saturated 0.5 M $KHCO_3$ solution are shown in **Fig. 3c-d** and **Supplementary Fig. 18-19**.[47] As displayed in **Fig. 3c**, at open circuit potential (OCP), two characteristic Raman peaks at 1342 cm^{-1} and 1505 cm^{-1} were observed on SnPc/CNT-OH, which can be assigned to C=C and C-N vibrations of the phthalocyanine ring, respectively.[48] With potential decreasing from -0.7 to -1.2 V vs. RHE, the peak intensity of C=C and C-N gradually decreased and eventually vanished, which is most probably due to the generation of surface-bound tin-carbonate (bidentate) species with a symmetric structure. Upon switching the

electrode potential back to OCP, the Raman spectrum could almost be restored to that recorded under the initial OCP condition, suggesting that the potential-induced changes for the SnPc/CNT-OH catalyst are reversible. Moreover, *operando* Raman spectra measured in Ar-saturated 0.5 M $KHCO_3$ solution showed no significant changes in peak intensity, further reflecting that the observed reversible change of characteristic Raman peaks probably resulted from the *in situ* formation of surface-bound bidentate tin carbonate species, which was captured by the *operando* ATR-SEIRAS measurements.

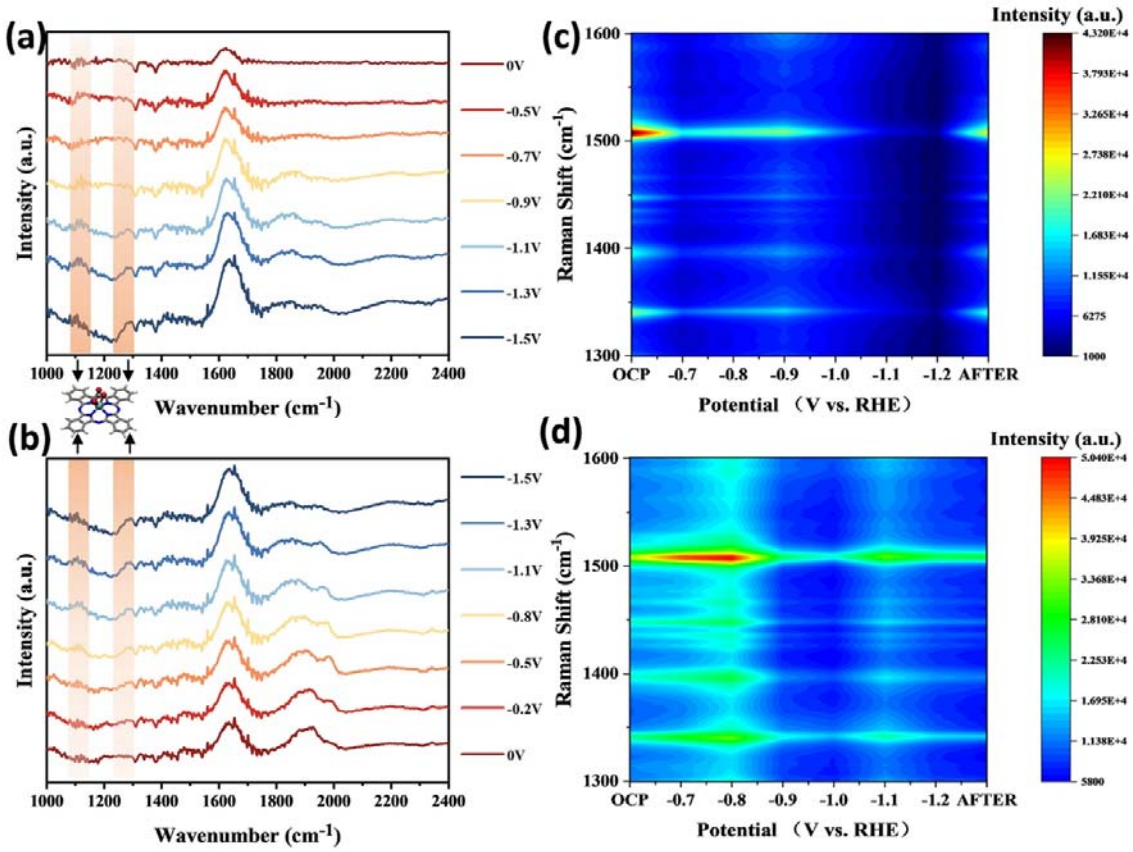

Fig. 3 | Identification of the surface reaction species, **a-b**, *Operando* ATR-SEIRAS spectra of SnPc/CNT-OH collected under various applied cathodic potentials (from 0 to -1.5 V vs. RHE and from -1.5 V vs. RHE to 0) in CO_2-saturated 0.1 M K_2SO_4. *Operando* Raman spectra recorded over SnPc/CNT-OH at various potentials (V vs. RHE) in **c**, CO_2-saturated and **d**, Ar-saturated 0.5 M $KHCO_3$ solution.

To further probe the structure of the catalytic intermediates, *operando* XAS measurements were performed. The Sn *K*-edge XANES and EXAFS spectra were recorded in CO_2-saturated 0.5 M $KHCO_3$ solution at various potentials. For the XANES spectra (**Fig. 4a**), a negligible reduction was observed for the Sn *K*-edge of SnPc/CNT-OH during the CO_2RR, revealing that the oxidation state of Sn in SnPc/CNT-OH could be maintained at Sn(IV). In addition, in the EXAFS spectra shown in **Fig. 4b**, the slight increase of the Sn-N (or Sn-C or Sn-O) intensity suggests an increase of the coordination number (CN) of Sn as the CO_2 reduction reaction proceeds. However, negligible changes in the Sn-N bond length were observed, indicating that the coordination environment did not change significantly during the CO_2RR.

The electronic and coordination structure of the single-Sn-atom species under CO_2RR conditions [47, 49, 50] were further investigated using *operando* ^{119}Sn Mössbauer spectroscopy in a home-made H-type *operando* cell (**Supplementary Fig. 20**). The CO_2-saturated 0.5 M $KHCO_3$ electrolyte was replaced every ~1.5 h to maintain the pH of the solution. The current-time response of SnPc/CNT-OH during the entire *operando* Mössbauer measurements was quite stable, supporting that the setup performs well and the *operando* spectroscopic data are reliable (**Supplementary Fig. 21**). As shown in **Fig. 4c**, at -1.1 V vs. RHE, the Mössbauer spectrum of SnPc/CNT-OH is different from that of the fresh sample, displaying a symmetric signal with an IS value of 0.03 mm s^{-1} and a QS value of 0.89 mm s^{-1}, matching well with the theoretical Mössbauer spectrum of Sn-O-CO_2 (**Fig. 4d)**. The experimental IS and QS values of the catalyst under various *operando* conditions as well as the theoretical IS and QS values of Sn-O-CO_2 are shown in **Fig. 4e** and **Supplementary Table 5**. The results support the *in situ* formation of Sn-O-CO_2 species over O-Sn-N_4 sites during CO_2RR. After removing the applied potential, the Mössbauer spectrum could be fitted by a quadrupole doublet with an IS value of 0.07 mm s^{-1} and a QS value of 0.50 mm s^{-1}, similar to that of the fresh SnPc/CNT-OH, further suggesting the reversibility of the single-Sn-atom species during the CO_2RR.

The dynamic changes observed in the *operando* Mössbauer and XAS measurements could be further illustrated by the calculated projected density of states (PDOS) of O-Sn-N_4 and Sn-O-CO_2. As shown in **Supplementary Fig. 22,** similar electron density encloses in the s and p orbital of Sn for O-Sn-N_4 and Sn-O-CO_2, which results in the negligible changes in the K-edge of *operando* XANES spectra and IS value of *operando* Mössbauer spectra. However, compared with Sn(IV) in O-Sn-N_4, the d orbitals (d_{xz} and d_{yz}) of Sn-O-CO_2 change from degeneration to non-degeneration (**Fig. 4f**), which leads to an increase in the asymmetric distribution of the electrons and thus an increase of QS. All these results clearly evidenced the *in-situ* formation of Sn-O-CO_2 species over O-Sn-N_4 sites during the CO_2RR.[24]

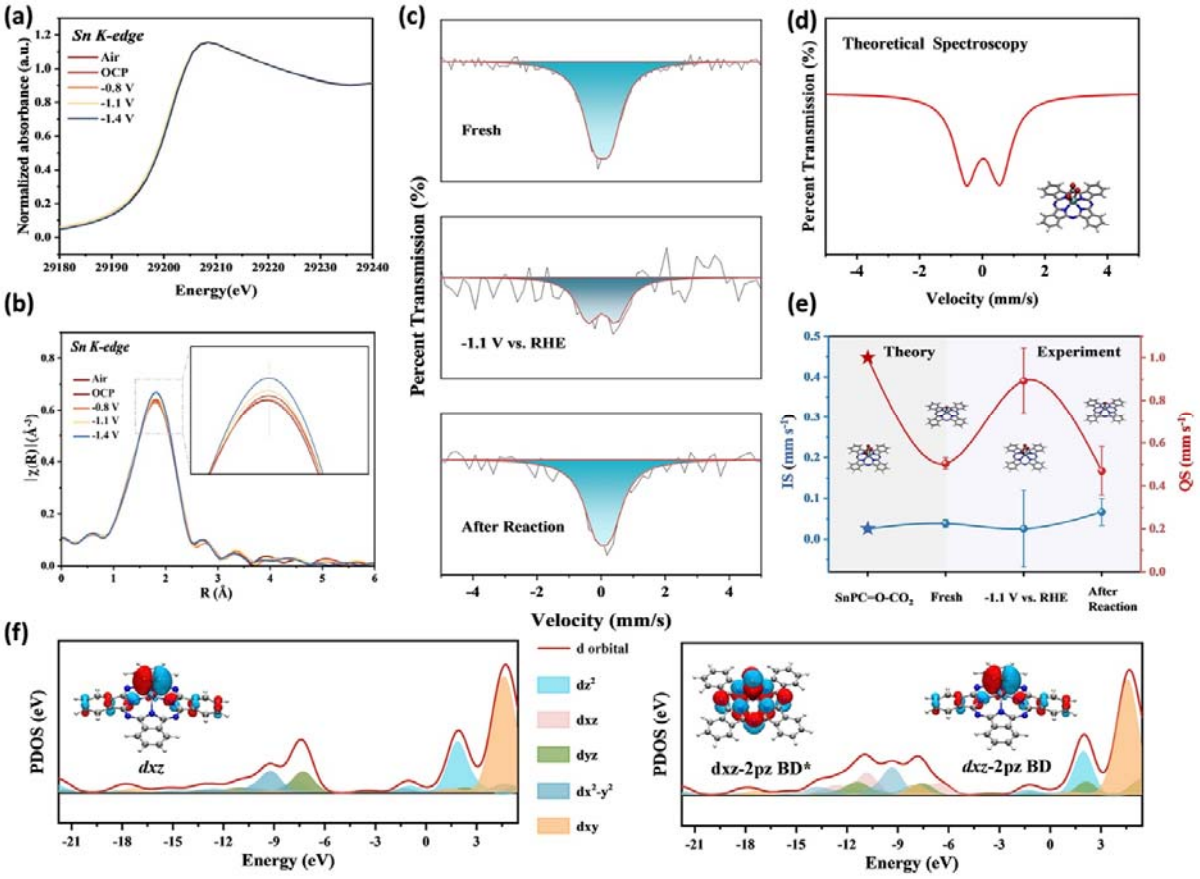

Fig. 4 | Identification of the catalytic intermediates. a, Normalized *operando* Sn K-edge XANES spectra**. b,** FT magnitude of EXAFS spectra of SnPc/CNT-OH during CO_2RR recorded in CO_2-

saturated 0.5 M $KHCO_3$ solution. **c,** *Operando* ^{119}Sn Mössbauer spectra for SnPc/CNT-OH recorded before CO_2RR (Fresh), at -1.1 V vs. RHE, and after CO_2RR (After Reaction) in CO_2-saturated 0.5 M $KHCO_3$ solution at room temperature. **d**; Theoretical ^{119}Sn Mössbauer spectrum of Sn-O-CO_2, **e**, Comparison of the experimental IS and QS values of the catalyst recorded under various conditions and the theoretical IS and QS values of Sn-O-CO_2 structural model (optimized by DFT). **f**, Schematic illustration showing the PDOS of Sn-d orbitals on O-Sn-N_4 and Sn-O-CO_2, respectively.

Theoretical insights into the catalytic mechanism

Theoretical calculations were performed to further investigate the mechanism of CO_2RR over the single-Sn-atom catalysts. The optimized structures of O-Sn-N_4 and Sn-N_4, and the possible adsorption configurations of reaction intermediates are shown in **Supplementary Fig. 23**. **Fig. 5a** shows the Kohn–Sham MO energy-level correlation diagram between CO_2 and the O-Sn-N_4 site during the first CO_2 capture step (* + CO_2 → *CO_2). There exist covalent overlaps between the fully occupied d_{z^2} orbital of the O-Sn-N_4 site and the non-occupied π* orbital of CO_2, generating one fully occupied d_{z^2}-π* bonding orbital (BD) and one empty d_{z^2}-π* antibonding (BD*) orbital. Similarly, the fully occupied d_{xz} orbital of the O-Sn-N_4 site and the $2p_z$ orbital of CO_2 also generate two fully occupied d_{xz}-$2p_z$ bonding orbital (BD) and d_{xz}-$2p_z$ antibonding (BD*) orbital. The corresponding MO contour plots of these MOs are displayed in **Supplementary Fig. 24**.

We further calculated the Gibbs free energy diagram of CO_2RR to form HCOOH and CO over O-Sn-N_4 and Sn-N_4. As shown in **Fig. 5b**, for the pathway of generating formic acid, the formation of the *HCOOH intermediate via *OCHO/HCOO* hydrogenation is the potential-limiting step; whereas, for producing CO (**Supplementary Fig. 25)**, the potential-limiting step is the formation of *COOH. The corresponding energy barriers of CO_2-to-HCOOH and CO_2-to-CO on O-Sn-N_4 and Sn-N_4 are summarized in **Fig. 5c.** Specifically, the downhill energy barrier of the first CO_2-to-*CO_2 step of CO_2RR on O-Sn-N_4 is calculated to be -0.58 eV, while Sn-N_4 exhibits a downhill energy barrier of -

0.13 eV, revealing that the CO_2 activation can take place more readily on O-Sn-N_4. Furthermore, O-Sn-N_4 exhibits a relatively lower energy barrier at the formation of *HCOOH (ΔG = 0.8 eV) than Sn-N_4 (ΔG = 0.93 eV), which shall lead to a higher electrocatalytic activity for CO_2RR to HCOOH over O-Sn-N_4. Additionally, Sn-N_4 displays a much stronger adsorption of *COOH with ΔG = 0.78 eV than O-Sn-N_4 with ΔG = 1.02 eV, resulting in a better catalytic ability for the generation of CO over Sn-N_4. As illustrated in **Supplementary Fig. 26-27**, we also assumed that CO_2 approached the single-Sn-atom sites from the back side of O-Sn-N_4 (O-Sn-N_4-inversion). From the Gibbs free-energy diagram, such a convex inversion shows a much higher energy barrier for the formation of both *COOH and *OCHO intermediates, thereby prohibiting both the HCOOH and CO production. Therefore, the reaction pathways of CO_2RR over O-Sn-N_4 and Sn-N_4 sites are presented in **Fig. 5d** and **Supplementary Fig. 28-29**. The O-Sn-N_4 species can regulate the adsorption configuration of *CO_2, which effectively reduces the energy barrier for the formation of *OCHO intermediate and facilitates the CO_2-to-HCOOH conversion.

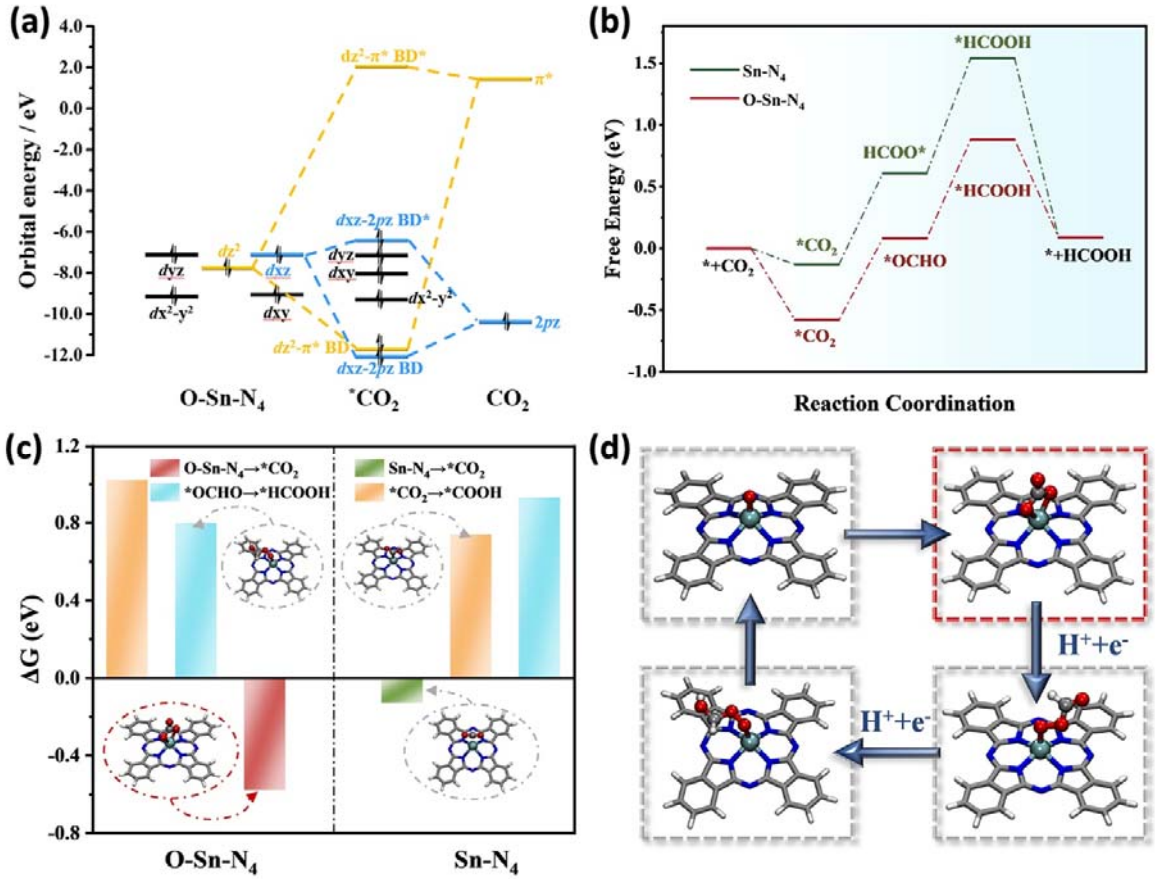

Fig. 5 | Theoretical calculations. **a,** Schematic Kohn–Sham molecular orbital (MO) energy-level correlation diagram between CO_2 and the O-Sn-N_4 site during the CO_2 capture step (* + CO_2 → *CO_2). **b,** Calculated Gibbs free energy diagrams for CO_2RR to HCOOH over O-Sn-N_4 and Sn-N_4 sites. **c,** Calculated ΔG for HCOOH and CO production over O-Sn-N_4 and Sn-N_4 sites. **d**, Proposed reaction pathway for CO_2RR over O-Sn-N_4 site.

Conclusions

In summary, a series of single-Sn-atom catalysts with well-controlled coordination and electronic structure were developed to explore the CO_2 reduction chemistry. Using a combination of *operando* spectroscopies and DFT calculations on a model single-Sn-atom catalyst in which all Sn atoms are in a positive IV oxidation state, situated in a phthalocyanine ring and additionally coordinated to an axial

oxygen species (O-Sn-N_4), the *in situ* generation of surface-bound bidentate tin carbonate species (Sn-O-CO_2) in CO_2RR was captured and the dynamic change of the electronic and coordination structures of active sites during CO_2RR was identified. Theoretical studies further revealed that the O-Sn-N_4 species could regulate the adsorption configuration of *CO_2 with increasing the asymmetric distribution of the d orbital electrons of Sn(IV), reducing the energy barrier for the formation and hydrogenation of *OCHO species, thus facilitating CO_2-to-HCOOH conversion. The results of this work provide an in-depth understanding of the detailed structures of catalytic intermediates and the key surface species associated with CO_2RR and shall pave the way towards the rational design of high-performance CO_2 electroreduction catalysts.

AUTHOR INFORMATION

Corresponding authors

*lixn@dicp.ac.cn (X.L.)

*yqhuang@dicp.ac.cn (Y.H.)

*liubin@ntu.edu.sg (B.L.)

Author Contributions

Y.C.D., J.Z. and S.F.W. contributed equally to this work. Y.C.D., X.N.L., Y.Q.H. and B.L. designed the study. Y.C.D. synthesized and characterized the materials. J.Z. performed the density functional theory calculations. Y.C.D. and S.F.W. conducted the electrochemical measurements and analysis. Y.C.D. and S.F.W. performed the Raman spectroscopy measurements and analysis. Y.C.D. and J.D. conducted the ATR-SEIRAS measurements and analysis. H.J.T., W.J.Z., S.F.H. and W.X. performed the XAFS measurements and analysis. Y.C.D., S.F.W. R.R.C., J.H.W. and X.N.L. conducted the Mössbauer spectroscopy measurements and analysis. J.H.W. and F.J. participated in the modification of the Results and Discussion section. Y.C.D., X.N.L. and B.L. wrote and edited the manuscript with inputs from all authors. The project was supervised by X.N.L., Y.Q.H. and B.L.

Notes

The authors declare no competing financial interests.

ASSOCIATED CONTENT

Supporting Information

Supplementary data associated with this article is available free of charge via the Internet at www.nature.com/reprints.

Acknowledgements

This work was financially supported by the National Key Research and Development Program of China (No. 2021YFA1500502), the National Natural Science Foundation of China (22102176, U19A2015 and 21925803), CAS Project for Young Scientists in Basic Research (YSBR-051), the Strategic Priority Research Program of the Chinese Academy of Sciences (XDB36030200), Ministry of Education of Singapore (Tier 1: RG4/20 and Tier 2: MOET2EP10120-0002), and Agency for Science, Technology and Research (AME IRG: A20E5c0080). The authors gratefully acknowledge the support of Photon Science Center for Carbon Neutrality.

REFERENCES

1. Murthy PS, Liang W, Jiang Y & Huang J. Cu-Based Nanocatalysts for CO_2 Hydrogenation to Methanol. *Energ. Fuel.* **35**, 8558-8584 (2021).

2. Zu X, et al. Efficient and Robust Carbon Dioxide Electroreduction Enabled by Atomically Dispersed Sn(delta) (+) Sites. *Adv. Mater.* **31**, e1808135 (2019).

3. Fan L, Xia C, Zhu P, Lu Y & Wang H. Electrochemical CO_2 reduction to high-concentration pure formic acid solutions in an all-solid-state reactor. *Nat. Commun.* **11**, 3633 (2020).

4. Song Z, et al. Recent Advances in MOF-Derived Single Atom Catalysts for Electrochemical Applications. *Adv. Energy. Mater.* **10**, (2020).

5. Liu H, et al. Highly efficient CO_2 electrolysis within a wide operation window using octahedral tin oxide single crystals. *J. Mater. Chem. A.* **9**, 7848-7856 (2021).

6. Zhong H, et al. Synergistic electroreduction of carbon dioxide to carbon monoxide on bimetallic layered conjugated metal-organic frameworks. *Nat. Commun.* **11**, 1409 (2020).

7. Woldu AR, Huang Z, Zhao P, Hu L & Astruc D. Electrochemical CO_2 reduction (CO_2RR) to multi-carbon products over copper-based catalysts. *Coordin. Chem. Rev.* **454**, (2022).

8. Xie Y, et al. High carbon utilization in CO_2 reduction to multi-carbon products in acidic media. *Nat. Catal.* **5**, 564-570 (2022).

9. Banerjee S, Gerke CS & Thoi VS. Guiding CO_2RR Selectivity by Compositional Tuning in the Electrochemical Double Layer. *Acc. Chem. Res.* **55**, 504-515 (2022).

10. Ni W, et al. Nonnitrogen Coordination Environment Steering Electrochemical CO_2-to-CO Conversion over Single-Atom Tin Catalysts in a Wide Potential Window. *ACS. Catal.* **11**, 5212-5221 (2021).

11. Vijay S, et al. Unified mechanistic understanding of CO_2 reduction to CO on transition metal and single atom catalysts. *Nat. Catal.* **4**, 1024-1031 (2021).

12. Qin X, Zhu S, Xiao F, Zhang L & Shao M. Active Sites on Heterogeneous Single-Iron-Atom Electrocatalysts in CO_2 Reduction Reaction. *ACS. Energy. Lett.* **4**, 1778-1783 (2019).

13. Shi Y, et al. Unveiling hydrocerussite as an electrochemically stable active phase for efficient carbon dioxide electroreduction to formate. *Nat. Commun.* **11**, 3415 (2020).

14. Wei B, et al. Efficient electrocatalytic reduction of CO_2 to HCOOH by bimetallic In-Cu nanoparticles with controlled growth facet. *Appl. Catal. B:Environ.* **283**, 119646 (2021).

15. Wu Z, et al. Engineering Bismuth-Tin Interface in Bimetallic Aerogel with a 3D Porous Structure for Highly Selective Electrocatalytic CO_2 Reduction to HCOOH. *Angew. Chem. Int. Ed.* **60**, 12554-12559 (2021).

16. Yang X, Lee JH, Kattel S, Xu B & Chen JG. Tuning Reaction Pathways of Electrochemical Conversion of CO_2 by Growing Pd Shells on Ag Nanocubes. *Nano. Lett.* **22**, 4576-4582 (2022).

17. Xie W, et al. NiSn Atomic Pair on an Integrated Electrode for Synergistic Electrocatalytic CO_2 Reduction. *Angew. Chem. Int. Ed.* **60**, 7382-7388 (2021).

18. Zheng T, et al. Copper-catalysed exclusive CO_2 to pure formic acid conversion via single-atom alloying. *Nat. Nanotechnol.* **16**, 1386-1393 (2021).

19. Qiao Y, et al. Engineering the Local Microenvironment over Bi Nanosheets for Highly Selective Electrocatalytic Conversion of CO_2 to HCOOH in Strong Acid. *ACS. Catal.* **12**, 2357-2364 (2022).

20. Huang B, Song L, Liang Z, Sun M & Du YP. Interfacial Effect induced by Rare Earth Oxide in Boosting Conversion of CO_2 to Formate. *Energ. Environ. Sci.* (2022).

21. Ma W, et al. Promoting electrocatalytic CO_2 reduction to formate via sulfur-boosting water activation on indium surfaces. *Nat. Commun.* **10**, 892 (2019).

22. Chi LP, et al. Stabilizing indium sulfide for CO_2 electroreduction to formate at high rate by zinc incorporation. *Nat. Commun.* **12**, 5835 (2021).

23. Zhao S, et al. Advances in Sn-Based Catalysts for Electrochemical CO_2 Reduction. *Nano-micro Lett.* **11**, 62 (2019).

24. Wang W, et al. In Situ Phase Separation into Coupled Interfaces for Promoting CO_2 Electroreduction to Formate over a Wide Potential Window. *Angew. Chem. Int. Ed.* **60**, 22940-22947 (2021).

25. Chen M, et al. Dynamic Restructuring of Cu-Doped SnS_2 Nanoflowers for Highly Selective Electrochemical CO_2 Reduction to Formate. *Angew. Chem. Int. Ed.* **60**, 26233-26237 (2021).

26. Ko YJ, et al. Exploring dopant effects in stannic oxide nanoparticles for CO_2 electro-reduction to formate. *Nat. Commun.* **13**, 2205 (2022).

27. Li Y, et al. Atomically Dispersed Dual-Metal Site Catalysts for Enhanced CO_2 Reduction: Mechanistic Insight into Active Site Structures. *Angew. Chem. Int. Ed.* **61**, e202205632 (2022).

28. Ren B, et al. Nano-crumples induced Sn-Bi bimetallic interface pattern with moderate electron bank for highly efficient CO_2 electroreduction. *Nat. Commun.* **13**, 2486 (2022).

29. He Y, Jiang W-J, Zhang Y, Huang L-B & Hu J-S. Pore-structure-directed CO2 electroreduction to formate on SnO2/C catalysts. *J. Mater. Chem. A.* **7**, 18428-18433 (2019).

30. Ju W, et al. Understanding activity and selectivity of metal-nitrogen-doped carbon catalysts for electrochemical reduction of CO_2. *Nat. Commun.* **8**, 944 (2017).

31. Li J, et al. Volcano Trend in Electrocatalytic CO_2 Reduction Activity over Atomically Dispersed Metal Sites on Nitrogen-Doped Carbon. *ACS. Catal.* **9**, 10426-10439 (2019).

32. Yang J, et al. Dynamic Behavior of Single-Atom Catalysts in Electrocatalysis: Identification of Cu-N_3 as an Active Site for the Oxygen Reduction Reaction. *J .Am. Chem. Soc.* **143**, 14530-14539 (2021).

33. Pan F, et al. Unveiling Active Sites of CO_2 Reduction on Nitrogen-Coordinated and Atomically Dispersed Iron and Cobalt Catalysts. *ACS. Catal.* **8**, 3116-3122 (2018).

34. Li XN, et al. Identification of the Electronic and Structural Dynamics of Catalytic Centers in Single-Fe-Atom Material. *Chem* **6**, 3440-3454 (2020).

35. Huang Y, et al. Mechanistic understanding and design of non-noble metal-based single-atom catalysts supported on two-dimensional materials for CO_2 electroreduction. *J. Mater. Chem. A.* **10**, 5813-5834 (2022).

36. Wu Y, et al. Boosting CO_2 Electroreduction over a Cadmium Single-Atom Catalyst by Tuning of the Axial Coordination Structure. *Angew. Chem. Int. Ed.* **60**, 20803-20810 (2021).

37. Creissen CE & Fontecave M. Keeping sight of copper in single-atom catalysts for electrochemical carbon dioxide reduction. *Nat. Commun.* **13**, 2280 (2022).

38. Xie W, et al. NiSn Atomic Pair on an Integrated Electrode for Synergistic Electrocatalytic CO_2 Reduction. *Angew. Chem. Int. Ed.* **60**, 7382-7388 (2021).

39. Zhang X, et al. Highly selective and active CO_2 reduction electrocatalysts based on cobalt phthalocyanine/carbon nanotube hybrid structures. *Nat. Commun.* **8**, 14675 (2017).

40. Geng W, et al. Enhanced CO_2 electroreduction to formate over tin coordination polymers via amino-functionalization. *J. Power. Sources.* **529**, 231252 (2022).

41. Gabaudan V, et al. SnSb vs. Sn: improving the performance of Sn-based anodes for K-ion batteries by synergetic alloying with Sb. *J. Mater. Chem. A.* **7**, 15262-15270 (2019).

42. O'Rourke M & Curran C. Mossbauer Spectra of Tin Complexes of Phthalocyanine and Tetraarylporphines. *J. Am. Chem. Soc.* **92**, 1501-1505 (1970).

43. Liu S, et al. Identifying Active Sites of Nitrogen-Doped Carbon Materials for the CO_2 Reduction Reaction. *Adv. Funct. Mater.* **28**, 1800499 (2018).

44. Paul S, et al. Influence of the Metal Center in M–N–C Catalysts on the CO_2 Reduction Reaction on Gas Diffusion Electrodes. *ACS. Catal.* **11**, 5850-5864 (2021).

45. Handoko AD, Wei F, Jenndy, Yeo BS & Seh ZW. Understanding heterogeneous electrocatalytic carbon dioxide reduction through operando techniques. *Nat. Catal.* **1**, 922-934 (2018).

46. Baruch MF, Pander JE, White JL & Bocarsly AB. Mechanistic Insights into the Reduction of CO_2 on Tin Electrodes using in Situ ATR-IR Spectroscopy. *ACS. Catal.* **5**, 3148-3156 (2015).

47. Wu Y, Liang Y & Wang H. Heterogeneous Molecular Catalysts of Metal Phthalocyanines for Electrochemical CO_2 Reduction Reactions. *Acc. Chem. Res.* (2021).

48. Zedler L, Krieck S, Kupfer S & Dietzek B. Resonance Raman Spectro-Electrochemistry to Illuminate Photo-Induced Molecular Reaction Pathways. *Molecules* **24**, (2019).

49. Chen JYC, et al. Operando Analysis of NiFe and Fe Oxyhydroxide Electrocatalysts for Water Oxidation: Detection of Fe^{4+} by Mössbauer Spectroscopy. *J. Am. Chem. Soc.* **137**, 15090-15093 (2015).

50. Luo F, et al. P-block single-metal-site tin/nitrogen-doped carbon fuel cell cathode catalyst for oxygen reduction reaction. *Nat .Mater.* **19**, 1215-1223 (2020).